



HAL
open science

Dynamical environments of relativistic binaries: The phenomenon of resonance shifting

Ivan I. Shevchenko, Guillaume Rollin, José Lages

► **To cite this version:**

Ivan I. Shevchenko, Guillaume Rollin, José Lages. Dynamical environments of relativistic binaries: The phenomenon of resonance shifting. *Physical Review D*, 2019, 100 (6), pp.064016. 10.1103/PhysRevD.100.064016 . hal-02309006

HAL Id: hal-02309006

<https://hal.science/hal-02309006>

Submitted on 5 Jul 2023

HAL is a multi-disciplinary open access archive for the deposit and dissemination of scientific research documents, whether they are published or not. The documents may come from teaching and research institutions in France or abroad, or from public or private research centers.

L'archive ouverte pluridisciplinaire **HAL**, est destinée au dépôt et à la diffusion de documents scientifiques de niveau recherche, publiés ou non, émanant des établissements d'enseignement et de recherche français ou étrangers, des laboratoires publics ou privés.

Dynamical environments of relativistic binaries: The phenomenon of resonance shifting

Ivan I. Shevchenko^{1,2,3,*}, Guillaume Rollin,⁴ and José Lages⁴

¹*Pulkovo Observatory, Russian Academy of Sciences, 196140 Saint Petersburg, Russia*

²*Saint Petersburg State University, 7/9 Universitetskaya naberezhnaya, 199034 Saint Petersburg, Russia*

³*Lebedev Physical Institute, Russian Academy of Sciences, 119991 Moscow, Russia*

⁴*Institut UTINAM, Observatoire des Sciences de l'Univers THETA, CNRS, Université de Bourgogne Franche-Comté, Besançon 25030, France*



(Received 6 June 2019; published 9 September 2019)

In this article, we explore both numerically and analytically how the dynamical environments of mildly relativistic binaries evolve with increasing the general relativity factor γ (the normalized inverse of the binary size measured in the units of the gravitational radius corresponding to the total mass of the system). Analytically, we reveal a phenomenon of the relativistic shifting of mean-motion resonances: on increasing γ , the resonances between the test particle and the central binary shift, due to the relativistic variation of the mean motions of the primary and secondary binaries and the relativistic advance of the tertiary's pericenter. To exhibit the circumbinary dynamics globally, we numerically integrate equations of the circumbinary motion of a test particle and construct relevant scans of the maximum Lyapunov exponents and stability diagrams in the “pericentric distance–eccentricity” plane of initial conditions. In these scans and diagrams, regular and chaotic domains are identified straightforwardly. Our analytical and numerical estimates of the shift size are in a good agreement. Prospects for identification of the revealed effect in astronomical observations are discussed.

DOI: [10.1103/PhysRevD.100.064016](https://doi.org/10.1103/PhysRevD.100.064016)

I. INTRODUCTION

Any gravitating binary with the mass parameter (ratio of masses of the companions) greater than a specific threshold has a zone of chaos around it, where all circumbinary orbits of low-mass particles, irrespective of their eccentricities, are chaotic, due to accumulation of integer mean-motion resonances to the parabolic separatrix [1]. This underlines the importance of consideration of circumbinary resonant phenomena in actual astrophysical situations.

If any gravitating binary, whose dynamical environments are under study, is massive and close enough, one has to take into account effects of general relativity. Some aspects of resonant and chaotic orbital dynamics around relativistic binaries were explored by means of numerical experiments in [2–4]. In [2], an evolution of a massive black hole binary with a resonantly trapped circumbinary neutron star was studied. In [3], a specific resonance between the relativistic precession of a binary and the orbital motion of a distant third body around the binary was analyzed. Evolving chaotic dynamics of a test particle orbiting around a decaying (due to the gravitational radiation) relativistic binary was considered in [4].

In this article, we focus on resonant circumbinary phenomena. Namely, we explore the dynamical environments of mildly relativistic binaries, with an emphasis on analyzing the resonant structure of the border of the circumbinary chaotic zone.

A paradigmatic example of a relativistic binary is the black hole binary GW150914 shrinking before the merger: a transient gravitational-wave signal was observed by the Laser Interferometer Gravitational-Wave Observatory (LIGO) in 2015; it was attributed to the merger of two black holes [5–7]. In the source frame, the initial masses of the two merging black holes were estimated to have been $m_1 \sim 36$ and $m_2 \sim 29$ Solar masses [5]. New discoveries in this rapidly developing field of astronomy emerge [8]; therefore, theoretical studies of the premerger evolution, starting from mildly relativistic phases, of such and similar objects are actual. GW150914 represents just an example where circumbinary resonant phenomena can be present. Although circumbinary matter was not observed directly in the case of GW150914, it is inherent (in the form of planets and disks) to close stellar binaries, including binaries that have compact objects as components. Much more details and examples are given below in Sec. V.

In this article, we restrict our analysis to solely mildly relativistic binaries. Analytically, we reveal a phenomenon of resonance shifting in the dynamical vicinity of a

*iis@gaoran.ru

relativistic binary: on increasing γ (the normalized inverse of the binary size measured in the units of the gravitational radius corresponding to the total mass of the system), the mean-motion resonances between the test particle and the central binary shift slowly, due to the relativistic variation of the mean motions and the relativistic periastron advance. We derive formulas predicting this phenomenon analytically, construct relevant scans of Lyapunov exponents and stability diagrams, and compare the obtained numerical results with our theoretical predictions.

The paper is organized as follows. In Secs. II and III, a general theoretical approach to the effect of the relativistic shifting of circumbinary mean-motion resonances is given. In Sec. IV, we describe our numerical experiments, present Lyapunov exponent scans and stability diagrams, and compare the numerical results with the theoretical predictions. In Sec. V, prospects for astronomical observations of resonance shifts in the dynamics around relativistic binaries are considered. Section VI is devoted to the general discussion and conclusions.

II. RESONANT CIRCUMBINARY DYNAMICS

In the given problem, mean-motion resonances [9,10] correspond to commensurabilities between the orbital frequencies of the primary binary and an orbiting test particle. In the case of the particle's circumbinary motion, one has $a > a_b$, where a and a_b are the particle's and the binary's semimajor axes, respectively. We consider mean-motion resonances of the form $(k+q)/k$, where k and q are integers, and we set $1-k \leq q \leq -1$ and $k \geq 3$. Therefore, in what follows, q is always negative. The integer $|q|$ is the order of the resonance.¹ Therefore, the ratio of the particle's and binary's orbital frequencies is close to $(k+q)/k = (k-|q|)/k$ and is less than one.

Extending the analysis presented in [11,12], the Hamiltonian of a particle's motion in the vicinity of a mean-motion particle-binary resonance $(k+q)/k$ in the restricted elliptic planar three-body problem can be written as

$$H = \frac{1}{2}\beta\Lambda^2 - \sum_{p=q}^{p=0} \phi_{k+q,k+p,k} \cos(\psi + p\varpi), \quad (1)$$

where $\beta = 3k^2/a^2$, $\Lambda = \Psi - \Psi_{\text{res}}$, $\Psi = (\mu_1 a)^{1/2}/k$, $\Psi_{\text{res}} = (\mu_1^2/(k^2(k+q)n_b))^{1/3}$, and $\mu_1 = 1 - \mu$, $\mu = m_2/(m_1 + m_2)$ (we set $m_1 > m_2$); ϖ is the longitude of the particle's pericenter; $\psi = kl - (q+k)l_b$, where l and l_b are the mean longitudes of the particle and the binary, respectively. Note that index $p \leq 0$.

The units are chosen in such a way that the total mass of the primary (central) binary, the gravitational constant, and

the primary binary's semimajor axis a_b are all equal to one. The primary binary's mean longitude $l_b = n_b t$, and the primary binary's mean motion $n_b = 1$; i.e., the time unit equals $\frac{1}{2\pi}$ th part of the binary's orbital period.

Model (1) represents a truncated expansion of the original Hamiltonian, as expressed in resonance canonical Delaunay variables [10], in the Laplace series in the vicinity of a given high-order ($|q| \gtrsim 2$) mean-motion resonance; the expansion is truncated by ignoring the rapidly oscillating and small-amplitude terms. In [11,12], the model was demonstrated to provide a good description of the close-to-resonant dynamical behavior, if its applicability conditions are satisfied; see also comments to formula (4) below.

If the central binary is eccentric (the primary binary's eccentricity $e_b > 0$), resonance $(k+q)/k = (k-|q|)/k$ splits in a cluster of $|q|+1$ subresonances $p = 0, -1, -2, \dots, q$. The resonant argument of each subresonance is given by

$$\begin{aligned} \phi &= \psi + p\varpi = kl - (q+k)l_b + p\varpi \\ &= kl - (k-|q|)l_b - |p|\varpi, \end{aligned} \quad (2)$$

where $p = 0, -1, -2, \dots, q$.

At $q = 1 - k$, one has integer resonances (the binary's and particle's periods are in the ratio $1/k$, while their mean motions are in the integer ratio $k/1$). At $k \geq 2$, each of them splits (if $e_b > 0$) into a cluster of k subresonances with the arguments

$$\phi = kl - l_b + p\varpi \quad (3)$$

with $p = 0, -1, -2, \dots, 1 - k$.

The coefficients of the subresonant terms are given by

$$|\phi_{k+q,k+p,k}| \approx \frac{\mu}{|q|\pi a} \binom{|q|}{|p|} \left(\frac{\epsilon}{2}\right)^{|p|} \left(\frac{\epsilon_b}{2}\right)^{|q|-|p|}, \quad (4)$$

where $\epsilon = ea/|a - a_b|$ and $\epsilon_b = e_b a/|a - a_b|$; a_b and e_b are the primary binary's semimajor axis and eccentricity, respectively; a and e are the particle's semimajor axis and eccentricity, respectively.

In any application, formula (4) can be considered to provide a satisfactory qualitative precision, if $\epsilon|q| < 1$ [11]. Besides, as already noted above, model (1) is restricted to the resonances of relatively high order: $|q| \gtrsim 2$.

The frequency of small-amplitude oscillations on subresonance $|p|$ is given by

$$\begin{aligned} \omega_0 &= (\beta|\phi_{k+q,k+p,k}|)^{1/2} \\ &\approx \frac{a}{|a - a_b|} n_b \left[\mu_1 \mu \frac{4|q|}{3\pi} \binom{|q|}{|p|} \left(\frac{a}{a_b}\right) \left(\frac{\epsilon}{2}\right)^{|p|} \left(\frac{\epsilon_b}{2}\right)^{|q|-|p|} \right]^{1/2}. \end{aligned} \quad (5)$$

According to Eq. (4), if the central binary is circular (its eccentricity is zero), only one subresonance persists, the last one (that with $|q| = |p|$).

¹Note that the letter q is also used, traditionally, to designate the pericentric distance.

As it is clear, e.g., from Eq. (3), the apsidal precession may influence the location of resonances. Therefore, let us consider the relevant effects invoking the precession in the given dynamical configuration. There exist a number of causes for the apsidal precession, among them general relativity. A relatively rapid apsidal precession in our Solar System is exhibited by Mercury. The rate of Mercury's apsidal precession due to perturbations from all other planets is equal to 532'' per century; general relativity adds 43'' per century (see, e.g., [13]), whereas the Solar oblateness and tidal effects are negligible.

Einstein's formula for the relativistic apsidal precession rate of a particle orbiting around single central mass M is

$$\omega_E \equiv \dot{\omega} = \frac{6\pi\mathcal{G}M}{c^2 a(1-e^2)} = \frac{3\pi R_g}{q(1+e)} \quad (6)$$

(in radians per particle's orbital revolution) [13], where \mathcal{G} is the gravitational constant, c is the speed of light, and a and e are the semimajor axis and eccentricity of the particle's orbit, respectively; the gravitational radius R_g of the central mass M is equal to $2\mathcal{G}M/c^2$.

For the classical nonrelativistic case, approximate analytical expressions describing the secular dynamics in the hierarchical circumstellar and circumbinary systems can be found in [14–16]. In the hierarchical circumbinary version of the circular ($e_b = 0$) restricted planar three-body problem, the apsidal precession rate of a circumbinary passively gravitating tertiary, in ratio to the particle's mean motion n , is given by

$$\begin{aligned} \frac{\omega_{cl}}{n} &= \frac{3}{4} \frac{m_1 m_2}{(m_1 + m_2)^2} \left(\frac{a_b}{a}\right)^2 \\ &= \frac{3}{4} \mu(1-\mu) \left(\frac{a_b}{q}\right)^2 (1-e)^2. \end{aligned} \quad (7)$$

Here the subindex “cl” of ω means “classical”; i.e., the problem is nonrelativistic. The barycentric frame is adopted; m_1 and m_2 are the masses of the binary components (we set $m_1 \geq m_2$); $\mu = m_2/(m_1 + m_2)$; a_b and e_b are the primary binary's semimajor axis and eccentricity, respectively; a , q , and e are the tertiary's semimajor axis, pericentric distance and eccentricity, respectively.

In circumbinary configurations, general relativity can contribute much to the apsidal precession of the tertiary, if the central binary is massive and close enough. In the hierarchical circumbinary problem one has $M = m_1 + m_2$ in Eq. (6); therefore

$$\frac{\omega_E}{n} = 3\gamma \frac{a_b}{q(1+e)}, \quad (8)$$

where the dimensionless parameter γ , as defined in [17], is given by

$$\begin{aligned} \gamma &= \frac{\mathcal{G}M_S}{c^2 a_E} \cdot \frac{(m_1 + m_2)}{a_b} \\ &= 9.870994 \times 10^{-9} \cdot \frac{(m_1 + m_2)}{a_b}, \end{aligned} \quad (9)$$

M_S is the Solar mass, a_E is the astronomical unit, a_b is the binary's size, m_1 and m_2 are in Solar units, and a_b is in astronomical units. From Eq. (9) we see that the γ factor is just the normalized inverse of the size of the binary measured in the units of the gravitational radius corresponding to the total mass of the system.

In the post-Newtonian (PN) formalism, Eq. (8) for the pericenter advance is valid in its first approximation. For the second PN approximation, relevant expressions can be found, e.g., in [18–23]. We adopt the formula as given in [19] and in [23], Eq. (A1), rewriting it in the form

$$\frac{\omega_{1PN+2PN}}{n} = \frac{\omega_E}{n} + \left(\frac{\omega_E}{n}\right)^2 \left(\frac{13}{6} + \frac{17}{12}e^2\right), \quad (10)$$

where ω_E is given by Eq. (8). As one may conclude from this formula, the 2PN term in Eq. (10) may start to compete with the 1PN term at large e and γ . Therefore, henceforth we restrict our analysis to relatively small eccentricities $e \lesssim 0.2$.

The ratio of the relativistic (1PN) precession rate and the classical precession rate, as follows from Eqs. (7) and (8), is given by

$$\frac{\omega_E}{\omega_{cl}} = \frac{4\gamma}{\mu(1-\mu)} \frac{q}{a_b} (1+e)^{-1} (1-e)^{-2}. \quad (11)$$

The relativistic apsidal precession around a gravitating binary also contains a contribution due to the rotation of the binary; this contribution is retrograde. If $m_2 \ll m_1$, the rate of the precession induced by the spin angular momentum L of the binary is given by

$$\frac{\omega_L}{n} = -\frac{4\mathcal{G}m_2 a_b^{1/2}}{c^2 a^{3/2} (1-e^2)^{3/2}}; \quad (12)$$

see Eqs. (A2) and (A3) in [24] and also [25]. Introducing γ and q in this formula, one has

$$\frac{\omega_L}{n} \simeq -4\mu\gamma \left(\frac{a_b}{q}\right)^{3/2} (1+e)^{-3/2}. \quad (13)$$

As revealed in [24], the rotating central binary induces also a quadrupole moment and the corresponding (much smaller) prograde precession rate is given by

$$\begin{aligned} \frac{\omega_Q}{n} &\simeq \left(6 + \frac{171}{8}e^2\right) \mu \frac{a_b^2}{a^3} \\ &= \left(6 + \frac{171}{8}e^2\right) \mu\gamma \left(\frac{a_b}{q}\right)^3 (1-e)^3, \end{aligned} \quad (14)$$

with accuracy $\sim e^4$. Thus, the total rate of the relativistic precession caused by the central binary is given by

$$\frac{\omega_{\text{rel}}}{n} = \frac{\omega_E}{n} + \frac{\omega_L}{n} + \frac{\omega_Q}{n}. \quad (15)$$

III. RELATIVISTIC SHIFTING OF CIRCUMBINARY RESONANCES: THEORY

The relativistic shifts of the mean motion n_1 of the central binary and the mean motion n_2 of the tertiary from their nominal values $n_1^{(0)}$ and $n_2^{(0)}$ can be calculated using Eqs. (6) and (7) in [17]; we rewrite these equations in the form

$$n_1 = \left(1 + \frac{\mu(1-\mu) - 3}{2} \gamma_1\right) n_1^{(0)}, \quad (16)$$

$$n_2 = \left(1 - \frac{3}{2} \gamma_2\right) n_2^{(0)}, \quad (17)$$

where γ_1 and γ_2 are the values of the γ parameter calculated via Eq. (9), where a_b is set equal, respectively, to the semimajor axis of the central binary and to the semimajor axis of the tertiary's orbit. Designating the ratio of the orbital periods of the tertiary and the primary binary by f_T , one has for the value of this ratio shifted from the nominal location $f_T^{(0)}$

$$f_T \approx \left[1 + \frac{\mu(1-\mu)}{2} \gamma + \frac{3}{2} \left(\frac{1-e}{q} - 1\right) \gamma\right] f_T^{(0)}, \quad (18)$$

where $\gamma \equiv \gamma_1$ and q is measured in units of the primary binary size. Here it was taken into account that the correction is much less than the ratio itself. Designating the ratio of the semimajor axes by f_a , one has

$$f_a \approx \left[1 + \frac{\mu(1-\mu)}{3} \gamma + \left(\frac{1-e}{q} - 1\right) \gamma\right] f_a^{(0)}. \quad (19)$$

For $e \sim 0$ and $q \gg 1$, these two formulas reduce to

$$f_T \approx \left(1 - \frac{3}{2} \gamma\right) f_T^{(0)} \quad (20)$$

and

$$f_a \approx (1 - \gamma) f_a^{(0)}. \quad (21)$$

Let us now calculate how the shift of resonance can be influenced by the relativistic apsidal precession. We consider the integer mean-motion resonances (the binary's and particle's periods are in the ratio $1/k$, while their mean motions are in the integer ratio $k/1$).

As follows from Eq. (4), in the circular ($e_b = 0$) restricted planar three-body problem only one subresonance is present in the mean-motion resonance multiplet, namely, that with $p = 1 - k$. The resonance is therefore not split and is represented in the sum (1) solely by the term with $p = 1 - k$. For the system to be in resonance, the averaged time derivative of the resonant argument, given by Eq. (3), should be equal to zero: $k\dot{l} - \dot{l}_b + (1 - k)\dot{\omega} = 0$. Therefore, the location of an integer mean-motion resonance is given by

$$\frac{n_{\text{res}}}{n_b} = \frac{1}{k} + \frac{k-1}{k} \cdot \frac{\omega_\Sigma}{n_b}, \quad (22)$$

where the apsidal precession rate is the sum of the classical and relativistic contributions:

$$\omega_\Sigma = \omega_{\text{cl}} + \omega_{\text{rel}}. \quad (23)$$

In the following, we are interested in the resonance relativistic shift from the classical nominal location affected already by the classical circumbinary precession. Based on Eq. (23), it is straightforward to assess the amount of this shift:

$$f_T \approx \left[1 - (k-1) \frac{\omega_E}{n}\right] f_T^{(0)} \approx \left[1 - \frac{3(k-1)\gamma}{q(1+e)}\right] f_T^{(0)}, \quad (24)$$

where q is measured in units of the primary binary size. Analogously,

$$f_a \approx \left[1 - \frac{2(k-1)\gamma}{q(1+e)}\right] f_a^{(0)}. \quad (25)$$

At $e \sim 0$, one has

$$f_T \approx \left[1 - \frac{3(k-1)\gamma}{q}\right] f_T^{(0)} \quad (26)$$

and

$$f_a \approx \left[1 - \frac{2(k-1)\gamma}{q}\right] f_a^{(0)}. \quad (27)$$

The total shift in the semimajor axis is given by the sum of the shifts in (19) and (25):

$$\begin{aligned} \Delta f_a &\equiv \frac{f_a}{f_a^{(0)}} - 1 \\ &\approx \frac{\mu(1-\mu)}{3} \gamma + \left(\frac{1-e}{q} - 1\right) \gamma - \frac{2(k-1)\gamma}{q(1+e)}, \end{aligned} \quad (28)$$

or, at $e \sim 0$ and $q \gg 1$,

$$\Delta f_a \approx - \left[1 + \frac{2(k-1)}{q} \right] \gamma. \quad (29)$$

For example, assume that $e = 0$, $q = 2$, and $k = 3$; then from Eq. (28) follows $\Delta f_a \approx -2.5\gamma$ and from Eq. (29) follows $\Delta f_a \approx -3\gamma$.

Note that, as already mentioned above, in the case when the primary binary is circular ($e_b = 0$), solely the $p = 1 - k$ term is present in the multiplet; others are nonexistent (have zero coefficients) and, therefore, there is no need to consider them. Concerning half-integer and other higher-level (in the Farey tree defined below in Sec. IV) resonances, their shifts can be estimated as averages taken over their two integer neighbors in the Farey tree.

Concluding this section, one may summarize that the mean-motion resonances between the tertiary and the primary binary are subject to shifting from their nominal locations due to (i) the relativistic corrections to the mean motions of the central binary and the tertiary and (ii) the relativistic apsidal precession of the tertiary's orbit. In both cases, the shift in the period ratio or in the semimajor axis ratio is negative and is of the order of γ ; thus, the cumulative effect is also of the order of γ . The total shift can be calculated using Eq. (28) or (29).

IV. STABILITY DIAGRAMS

Our numerical simulations are performed in the framework of the circular restricted three-body planar problem in post-Newtonian approximation, adopting the equations of motion as given in [17]. The software code developed in [17] is used.

To distinguish between regular and chaotic types of motion in the given problem, we use a statistical method proposed and applied in [26,27]. It consists of four steps. (i) On a representative set of initial data, two differential distributions (histograms) of the orbits in the computed value of $\log_{10}\lambda_{\max}$ (where λ_{\max} is the maximum Lyapunov exponent) are constructed, using two different time intervals for the integration. (ii) If the phase space of motion is divided [28], each of these distributions has at least two peaks.

The peak that shifts (moves in the negative direction in the horizontal axis), when the integration time interval is increased, corresponds to the regular orbits. The peak (or a set of peaks) that stays still corresponds to the chaotic orbits. (iii) The value of $\log_{10}\lambda_{\max}$ at the histogram minimum between the peaks is identified, thus providing a numerical criterion for separating the regular motion from the chaotic one. (iv) The obtained criterion can be used in any further computations to identify regular or chaotic orbits on much finer initial data grids and, rather often, on smaller time intervals of integration. For the case of circumbinary motion, this method was implemented in [29] to construct stability diagrams of circumbinary planetary systems in the “ $q - e$ ” (pericentric distance–eccentricity) space of initial conditions of planetary orbits.

Henceforth, we adopt the following designations: T_r is the time of simulation (in orbital periods of the central binary), q is the initial pericentric distance (in units of the central binary size), $\mu \equiv m_2/(m_1 + m_2)$ is the mass parameter of the central binary ($m_2 < m_1$), and γ is the relativistic factor already defined.

In Fig. 1, we illustrate the limits of validity of the code used. The rate of precession of the pericenter of a particle's orbit around a single primary is shown as a function of the relativistic factor γ . (For a single primary, the relativistic factor γ is formally defined by setting the mass of the secondary to zero and the binary size to unity.) For all panels of the figure, the particle's pericentric distance $q = 3$. The eccentricities are (a) $e = 0.1$, (b) $e = 0.2$, and (c) $e = 0.3$. The dots represent the results of our numerical simulations, and the dashed straight line is the theoretical $\omega = 2\pi\frac{\omega_E}{n}$, where $\frac{\omega_E}{n}$ is given by Eq. (8).

One can see that the performance of the code improves with e decreasing: while at $e = 0.3$ the code sharply starts to produce a false retrograde precession at $\gamma > 0.003$, at $e = 0.1$ the precession starts to be retrograde much later, at $\gamma > 0.008$. Therefore, one may estimate and expect that at $e \approx 0$ the code is valid at γ values up to 0.01.

Our computations, performed separately at three relevant points of the diagram, namely, at ($q = 1.5$, $e = 0.01$), ($q = 2.0$, $e = 0.01$), and ($q = 2.2$, $e = 0.01$), confirm this

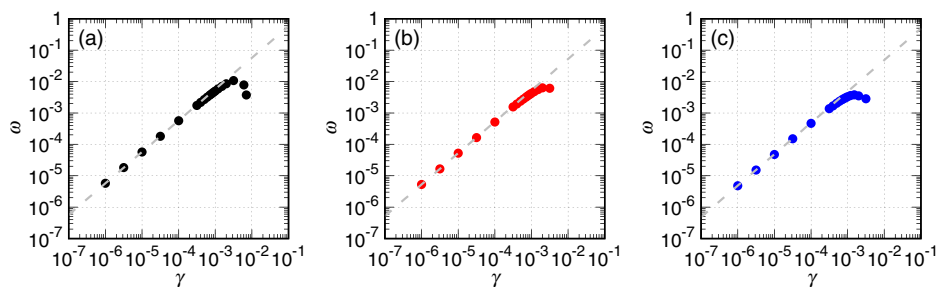


FIG. 1. The rate of apsidal precession of the particle's orbit around a single primary, as a function of the relativistic factor γ . For all panels, we set the particle's pericentric distance $q = 3$. The eccentricities: (a) $e = 0.1$, (b) $e = 0.2$, (c) $e = 0.3$. The dots represent the results of our numerical simulations, and the dashed straight line is the theoretical $\omega = 2\pi\frac{\omega_E}{n}$, where $\frac{\omega_E}{n}$ is given by Eq. (8).

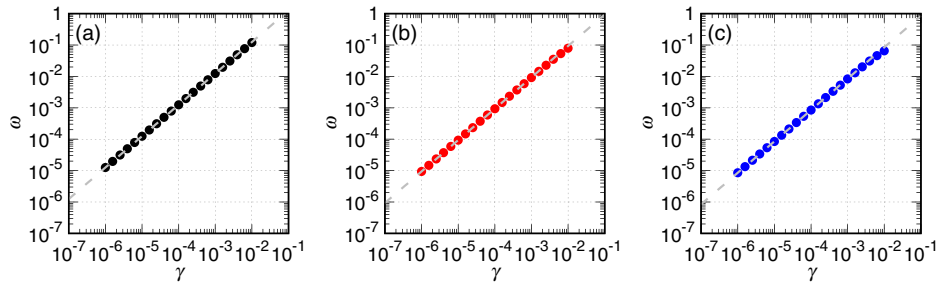


FIG. 2. The same as in Fig. 1, but at $e = 0.01$ (all panels) and $q = 1.5$ [panel (a)], $q = 2.0$ [panel (b)], and $q = 2.2$ [panel (c)].

expectation. In Fig. 2, the precession rate dependence on γ is shown for these three cases. The curves are apparently in a good agreement with the 1PN theory up to γ values as large as 0.01.

Now let us proceed to a numerical verification of the resonance shift phenomenon in the three-body problem. We set $\mu = 0.1$ and build two scans (one for $\gamma \approx 0$ and one for $\gamma = 0.01$) of the maximum Lyapunov exponent along the q axis at a small fixed e , namely, at $e = 0.01$. The scan's interval covers a relevant neighborhood of $q \sim 2$, namely, $q \in [1.5, 2.2]$. Note that Figs. 2(a) and 2(c) correspond to the borders of this interval. The scans are presented in Fig. 3. The black curve corresponds to $\gamma = 10^{-7}$, and the red one to $\gamma = 10^{-2}$. The 3/1 resonance chaotic band (at $q \approx 2$) is apparently shifted by the amount of ≈ -0.03 . As already calculated in Sec. III by means of Eq. (28), the theoretical $\Delta f_a \approx -2.5\gamma \approx -0.03$. The perfect agreement of the numerical-experimental result with the theory is evident; and the resonant shift phenomenon is thus confirmed numerically.

To provide a global picture of the circumbinary dynamics, we construct q - e stability diagrams (Fig. 4) in the given problem. In the upper panels of Fig. 4, the stability diagrams are presented for various γ values at fixed $\mu = 0.1$. Chaotic and regular zones in the plane of initial values of e and q are shown in red and blue, respectively.

These diagrams are presented here just for illustrative purposes, to provide a global overview of resonances.

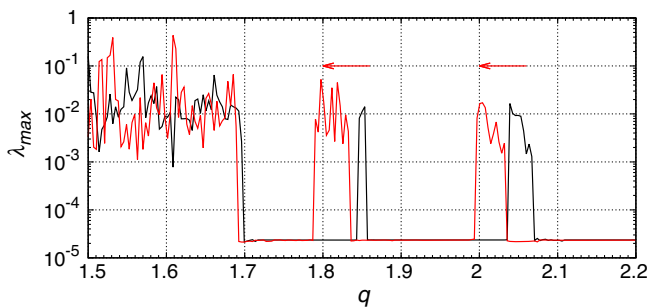


FIG. 3. Scans of the maximum Lyapunov exponent along the q axis at $e = 0.01$. The black curve corresponds to $\gamma = 10^{-7}$, and the red one to $\gamma = 10^{-2}$. The red arrows indicate the resonance shift direction.

The used code is not accurate enough to characterize resonance shifts at $\gamma = 0.01$ and $e = 0.1$ – 0.3 (i.e., in the upper part of the third panel in the figure). What is more, the deviations between the three panels cannot be used to quantify our effect, because it was described above analytically for the case of $e \approx 0$. However, at $e \approx 0$, the code is expected to perform accurately enough.

To distinguish between regular and chaotic orbits, the statistical method [26,27] is used, as described above. Namely, two values of the finite-time maximum Lyapunov exponent λ_{\max} are computed on a grid of initial values on two time intervals $T_r = 10^4$ and $T_r = 10^5$ (measured in the central binary revolutions); then, the λ_{\max} distributions are compared. The panels below the stability diagrams in Fig. 4 demonstrate the corresponding histograms of the maximum Lyapunov exponent λ_{\max} . The N/N_i value is the normalized relative number of orbits with the given λ_{\max} . The histograms are computed on fine grids of initial q and e , as prescribed above by the general algorithm of constructing such diagrams. Black and red curves correspond to the two computation times of 10^4 and 10^5 binary periods, respectively. The derived numerical criteria for the separation between regular and chaotic orbits are indicated in the histograms by dashed vertical lines. It is apparent that the fixed and shifted peaks are well separated (no overlap of them is present) and thus the regions of chaos and order are well defined.

The chaos border in Figs. 4(a)–4(c) is ragged due to resonances; the most prominent “teeth” (bands) correspond to integer resonances (the binary’s and particle’s periods are in the ratio $1/k$, while their mean motions are in the integer ratio $k/1$). The Farey tree [30] of the resonant teeth at the border is evident. Recall how the Farey tree is built: consider first the lowest-order “neighboring” ratios m/n and m'/n' [in the given case, these are the integer ratios $m/1$ and $(m+1)/1$]; then, the next (higher) level of the Farey tree is made of mediant given by the formula $m''/n'' = (m+m')/(n+n') = (2m+1)/2$. Thus the half-integer mean-motion resonances are the mediants for the integer ones, and so on. The orbital resonances accumulate more and more densely with increasing k , i.e., on approaching the parabolic separatrix; this effect is evident in the upper right parts of the panels in Fig. 4. Note that the shape of the resonant bands is essentially

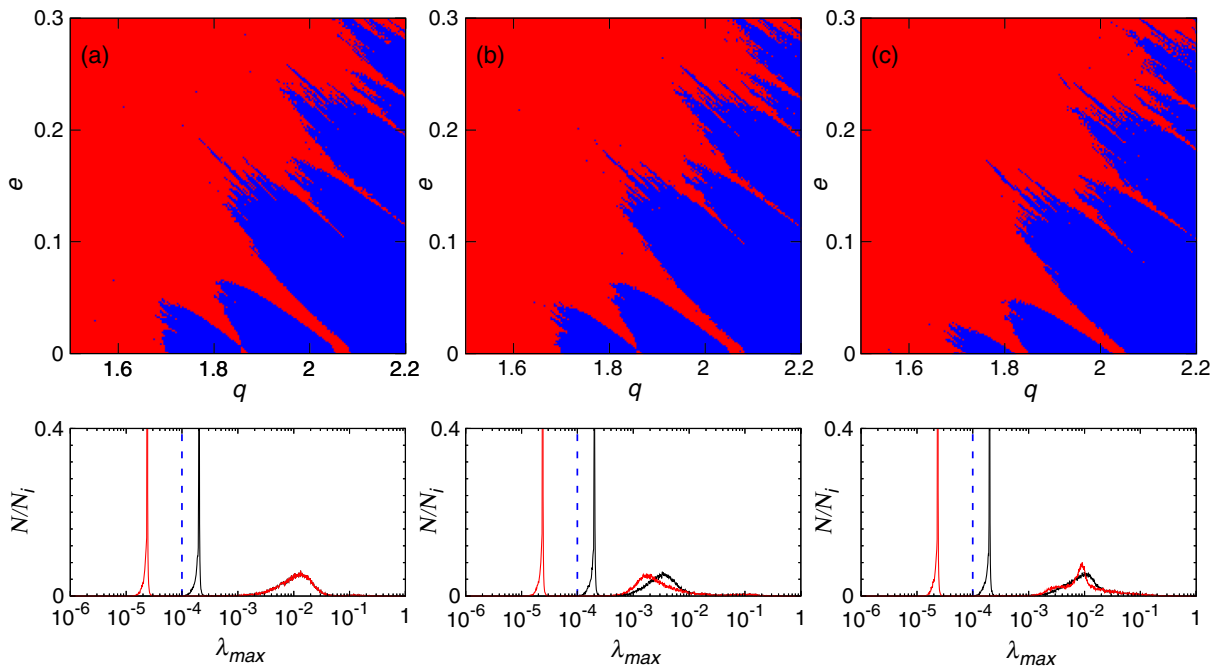


FIG. 4. Upper panels: “ q - e ” stability diagrams at fixed $\mu = 0.1$. Chaotic and regular zones are shown in red and blue, respectively. (a) $\gamma = 10^{-50} \sim 0$; (b) $\gamma = 10^{-3}$; (c) $\gamma = 10^{-2}$. Panels below: The corresponding histograms of computed values of Lyapunov exponents; see the text for details.

sensitive to variations of the system parameters; this is generic for marginal resonances; see [31]. Thus, the diagrams in Fig. 4 graphically demonstrate how major resonances interact and overlap.

As already mentioned above, at $e \approx 0$ the code is expected to perform accurately enough, and the resonance shifting phenomenon can be checked. Consider the resonant “tooth,” directed to the point ($q \approx 2$, $e = 0$). It corresponds to the mean-motion resonance 3/1. Comparing Figs. 4(b) and 4(c) (at $e \approx 0$, where the code is accurate), one may see that, on increasing γ by amount of 0.01, the tooth is shifted at this point to the left in the semimajor axis, by amount of ≈ -0.03 . Therefore, in this diagram, the numerical result again agrees with the analytical estimate already given above.

To illustrate the effect in a more general setting, in Fig. 5 we present a stability diagram constructed in the plane of values of the γ parameter and the initial value of q ; whereas $\mu = 0.1$ and $e = 0.01$. The method of construction is the same as for Fig. 4; the technical histogram of regular and chaotic orbits, not shown here, again demonstrates their perfect separation. In Fig. 5, the vicinity of the 3/1 resonance is displayed. Chaotic and regular zones are shown in red and blue, respectively. The white dashed curve is given by Eq. (28) at $k = 3$, $\mu = 0.1$, $e = 0.01$, and $q = 2.051$. We see that the resonance shift increases with γ and it generally follows the theoretical relation. At the highest values of γ (~ 0.01) in the diagram, the computed shift seems to be somewhat stronger than the theoretical one. This may be due to restrictions in both the theory and simulation code. To reveal graphically the code validity limits, in Fig. 6 we

present the normalized difference $(\omega - \omega_E)/\omega_E$ as a function of γ . Here ω is computed using the numerical code and ω_E is calculated by Eq. (8). The presented curves correspond to $q = 1.95$ and $q = 2.05$ (in the vicinity of the 3/1 resonance; see Fig. 5); $e = 0.01$. An artifact deviation of up to $\approx 16\%$ is seen at $\gamma = 0.01$. This deviation in ω may result in a deviation of up to $\approx 12\%$ in the total resonance shift at $\gamma = 0.01$, but the theory limitations come already into play at this level, as, e.g., we do not take into account the role of the binary’s

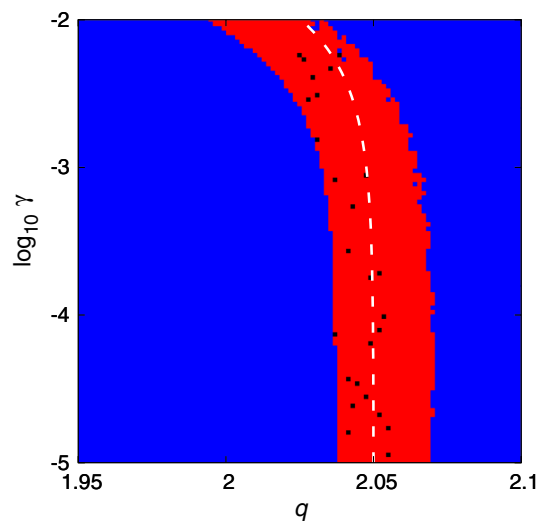


FIG. 5. The stability diagram γ vs q in the neighborhood of the 3/1 resonance. Chaotic and regular zones are shown in red and blue, respectively. The theoretical curve is white dashed.

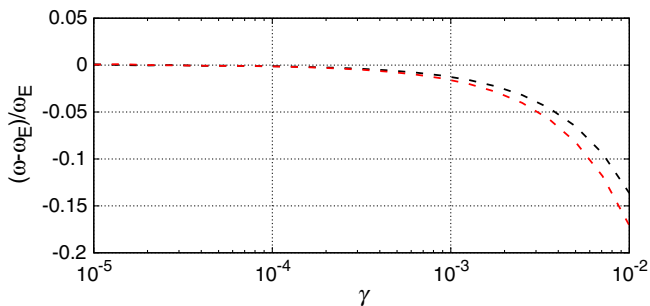


FIG. 6. The normalized difference $(\omega - \omega_E)/\omega_E$ as a function of γ . The numerical code is used to compute ω , and ω_E is calculated by Eq. (8). The black and red curves correspond to $q = 1.95$ and $q = 2.05$, respectively; $e = 0.01$.

angular momentum. Finally, we may conclude that the theory and simulation results are in a reasonable quantitative agreement.

V. OBSERVABILITY OF THE EFFECT

What are the prospects for astronomical observations of such resonance shifts in the dynamics of matter around relativistic binaries? Generally, circumbinary material is now routinely observed in the form of planets and disks [32,33]. Near-resonant circumbinary planets (CBPs) were identified [29,34], as well as resonant features in circumbinary disks; see, e.g., [35]. On the other hand, planetary systems of compact stars are known to be an ordinary phenomenon [33]. Moreover, historically, the first exoplanet was discovered in 1992 in a system of a neutron star (hereafter NS) [36]. Nowadays, the ubiquity of planets in orbits around such compact objects as single pulsars is well established. Tight binaries with compact components such as white dwarfs (hereafter WD) are observed that have CBPs [33]; a particular example is NN Ser.

As soon as the considered effect is proportional to γ , let us see, first of all, which binaries may have values of γ large enough. As given by Eq. (9), the γ factor is just the normalized inverse of the size of the binary measured in the units of the gravitational radius corresponding to the total mass of the system. Therefore, high values of γ are inherent to binaries that are tight and massive.

Merging black hole binaries, already mentioned in the introduction, such as GW150914, have $\gamma \sim 1$ at their late premerger stages of evolution; but any low-mass material around them (such as planets) is practically impossible to observe at the present technological level. There may exist relevant observationally verifiable mechanisms, such as production of free-floating planets, but considering such possibilities is far beyond the scope of our article.

Among the ordinary stellar binaries, the tightest ones are the so-called contact binaries, the W UMa-type stars. For them, the binary mass is ~ 2 Solar masses, and the binary size is ~ 2 Solar radii; therefore $\gamma \sim 10^{-6}$. This value should

be typical for yellow and red dwarf contact binaries, because for small main-sequence stars (M dwarfs) mass is approximately directly proportional to radius; see Table 1 in [37].

If we consider WD-WD and NS-NS binaries in close-to-contact configurations (not yet observed), we find that γ would be equal to $\sim 10^{-4}$ for a WD contact binary and ~ 0.1 for an NS contact binary (given that WD and NS masses are of order of a Solar mass and their radii are $\sim 10^4$ and ~ 10 km, respectively). These are the values that can be expected at late stages the inspiralling evolution of such binaries. If any close-to-resonant circumbinary planet were observed in such a system at this stage, its resonant shift can be identified by modern methods of exoplanetary studies, such as eclipse timing variation (ETV) or transit timing variation (TTV) methods in the case of WD-WD systems and the pulsar timing method in the case of NS-NS systems. (For descriptions of the methods see [33].) If any disk material were present, shifts of resonant features can also be searched for.

In principle, even for ordinary contact binaries (W UMa-type stars) the effect can be searched in the near future, because the TTV method already provides the relative precision of $\sim 10^{-4}$ in the determination of orbital periods of CBPs; see examples in [34,38].

Apart from stellar binaries, another relevant class of astrophysical objects, perspective from the observational viewpoint, is represented by supermassive black hole (SMBH) binaries in active galactic nuclei, such as OJ 287 and PKS 1302-102. The SMBH masses in active galactic nuclei can be as great as $\sim 10^{10}$ in Solar units, whereas the sizes of the SMBH binaries in OJ 287 and PKS 1302-102 are ~ 0.1 pc in the both cases [39,40]. Therefore, $\gamma \sim 0.01$ for both OJ 287 and PKS 1302-102. Resonance shifts can be searched in the dynamics of any material orbiting around the SMBH binaries, if such material were identified.

Concluding, two major classes of astrophysical objects, namely, (i) contact or close-to-contact stellar binaries and (ii) SMBH binaries in active galactic nuclei, represent perspective targets for astronomical observation and verification of the considered effect.

VI. DISCUSSION AND CONCLUSIONS

In this article, we have explored both numerically and analytically how the dynamical environments of mildly relativistic binaries may evolve with increasing the general relativity factor γ .

To exhibit the circumbinary dynamics globally, we have constructed, using direct numerical integrations, the q - e stability diagrams of the circumbinary orbits, in which any resonant and chaotic features can be straightforwardly identified.

Both analytically and numerically, we have revealed a new phenomenon of the relativistic shifting of mean-motion

resonances: on increasing γ , the main chaotic resonant bands (corresponding to integer resonances between the test particle and the central binary) shift, due to the relativistic corrections to the mean motions of the primary and secondary binaries and due to the relativistic advance of the tertiary's pericenter. We have derived formulas describing this phenomenon analytically. Our analytical and numerical estimates of the shift size agree well.

Apart from the theoretical and numerical-experimental aspects of the resonance shift phenomenon, we have considered prospects for its astronomical observation and verification. We find that two major classes of astrophysical objects, namely, (i) contact or close-to-contact stellar binaries and (ii) SMBH binaries in active galactic nuclei, are perspective for identifying the effect in observations.

Finally, we note that any numerical-experimental exploration of the resonant dynamical environments on further increasing γ requires much harder numerical simulation efforts, exploiting codes taking into account higher PN approximations. We leave this exploration for a future work. However, extrapolating the resonance shifting phenomenon to the domain of larger values of γ , i.e., physically, to harder relativistic inspiralling binaries, one may expect that, on increasing γ , the resonant bands would

further shift slowly closer to the central binary. Graphically, this phenomenon might be called a “sundew” effect, in analogy to a carnivorous plant that looks similar to the presented stability diagrams. The sundew effect might be important for the fate of any circumbinary matter (planets, planetesimals, dust, or dark matter particles), if present. The dynamical regular evolution of the matter between the slowly closing resonant teeth, as well as the chaotic evolution inside them, deserves a further numerical study.

ACKNOWLEDGMENTS

We express our deep gratitude to the referee, whose remarks helped to improve the manuscript. We are most grateful to Thomas Maindl for supplying us with the relativistic three-body integrator code. It is a pleasure to thank Dima Shepelyansky for helpful comments. I. I. S. was supported in part by the Russian Foundation for Basic Research (Project No. 17-02-00028) and by the Programmes of Fundamental Research of the Russian Academy of Sciences “Nonlinear dynamics: Fundamental problems and applications” and “Problems of origin and evolution of the Universe with application of methods of ground-based observations and space research” (CP19-270).

-
- [1] I. I. Shevchenko, *Astrophys. J.* **799**, 8 (2015).
 - [2] N. Seto and T. Muto, *Phys. Rev. D* **81**, 103004 (2010).
 - [3] N. Seto, *Mon. Not. R. Astron. Soc.* **430**, 558 (2013).
 - [4] G. Huang and X. Wu, *Gen. Relativ. Gravit.* **46**, 1798 (2014).
 - [5] B. P. Abbott *et al.* (Virgo and LIGO Scientific Collaborations), *Phys. Rev. Lett.* **116**, 061102 (2016).
 - [6] B. P. Abbott *et al.* (Virgo and LIGO Scientific Collaborations), *Phys. Rev. Lett.* **116**, 241103 (2016).
 - [7] B. P. Abbott *et al.* (Virgo and LIGO Scientific Collaborations), *Phys. Rev. X* **6**, 041015 (2016).
 - [8] B. P. Abbott *et al.* (Virgo and LIGO Scientific Collaborations), *Phys. Rev. Lett.* **118**, 221101 (2017).
 - [9] C. D. Murray and S. F. Dermott, *Solar System Dynamics* (Cambridge University Press, Cambridge, England, 1999).
 - [10] A. Morbidelli, *Modern Celestial Mechanics. Aspects of Solar System Dynamics* (Taylor & Francis, London, 2002).
 - [11] M. J. Holman and N. W. Murray, *Astron. J.* **112**, 1278 (1996).
 - [12] N. W. Murray and M. J. Holman, *Astron. J.* **114**, 1246 (1997).
 - [13] G. Clemence, *Rev. Mod. Phys.* **19**, 361 (1947).
 - [14] T. A. Heppenheimer, *Astron. Astrophys.* **65**, 421 (1978).
 - [15] K. Moriwaki and Y. Nakagawa, *Astrophys. J.* **609**, 1065 (2004).
 - [16] T. V. Demidova and I. I. Shevchenko, *Astrophys. J.* **805**, 38 (2015).
 - [17] T. I. Maindl and R. Dvorak, *Astron. Astrophys.* **290**, 335 (1994).
 - [18] C. Königsdörffer and A. Gopakumar, *Phys. Rev. D* **71**, 024039 (2005).
 - [19] C. Königsdörffer and A. Gopakumar, *Phys. Rev. D* **73**, 124012 (2006).
 - [20] M. Bagchi, *Mon. Not. R. Astron. Soc.* **428**, 1201 (2013).
 - [21] S. Mikkola and D. Merritt, *Astron. J.* **135**, 2398 (2008).
 - [22] M. Bonetti, F. Haardt, A. Sesana, and E. Barausse, *Mon. Not. R. Astron. Soc.* **461**, 4419 (2016).
 - [23] L. Dey *et al.* *Astrophys. J.* **866**, 11 (2018).
 - [24] K. Yamada and H. Asada, *Mon. Not. R. Astron. Soc.* **423**, 3540 (2012).
 - [25] L. D. Landau and E. M. Lifshitz, *The Classical Theory of Fields* (Pergamon Press, Oxford, 1971).
 - [26] A. V. Melnikov and I. I. Shevchenko, *Astronomicheskii Vestnik / Astronomy Review* **32**, 548 (1998) [*Solar System Research* **32**, 480 (1998)].
 - [27] I. I. Shevchenko and A. V. Melnikov, *Pis'ma Zh. Eksp. Teor. Fiz.* **77**, 772 (2003); [*JETP Lett.* **77**, 642 (2003)].
 - [28] B. V. Chirikov, *Phys. Rep.* **52**, 263 (1979).
 - [29] E. A. Popova and I. I. Shevchenko, *Astrophys. J.* **769**, 152 (2013).
 - [30] J. D. Meiss, *Rev. Mod. Phys.* **64**, 795 (1992).
 - [31] I. I. Shevchenko, *Phys. Rev. E* **85**, 066202 (2012).
 - [32] W. F. Welsh *et al.*, in *Formation, Detection, and Characterization of Extrasolar Habitable Planets, Proceedings of IAU Symposium 293*, edited by N. Haghighipour (Cambridge University Press, Cambridge, England, 2014), p. 125.

- [33] M. Perryman, *The Exoplanet Handbook* (Cambridge University Press, Cambridge, England, 2018).
- [34] L. R. Doyle *et al.*, *Science* **333**, 1602 (2011).
- [35] T. V. Demidova and I. I. Shevchenko, *Mon. Not. R. Astron. Soc.* **463**, L22 (2016).
- [36] A. Wolszczan and D. A. Frail, *Nature (London)* **355**, 145 (1992).
- [37] L. Kaltenegger and W. A. Traub, *Astrophys. J.* **698**, 519 (2009).
- [38] W. F. Welsh *et al.*, *Nature (London)* **481**, 475 (2012).
- [39] A. Sillanpää, S. Haarala, M. J. Valtonen, B. Sundelius, and G. G. Byrd, *Astrophys. J.* **325**, 628 (1988).
- [40] M. J. Graham, S. G. Djorgovski, D. Stern, E. Glikman, A. J. Drake, A. A. Mahabal, C. Donalek, S. Larson, and E. Christensen, *Nature (London)* **518**, 74 (2015).